

A Three Degree-of-Freedom Short-Stroke Lorentz-Force-Driven Planar Motor Using a Halbach Permanent Magnet Array with Unequal Thickness

He Zhang, Baoquan Kou, *Member, IEEE*, Hailin Zhang, and Yinxi Jin

Abstract—This paper presents a three degree-of-freedom (3-DOF) Lorentz-force-driven planar motor for a nanopositioning system. The short-stroke planar motor consists of three Lorentz-force-driven units equally spaced by 120 degrees around the mass center. To increase the force and decrease the force variation with horizontal displacement, a Halbach permanent magnet array with unequal thickness is used. First, the basic structure and 3-DOF kinematics of the planar motor are introduced. Second, the magnetic field and force expressions are derived based on the charge model and the image method. Third, four typical Lorentz-force-driven units are compared in the aspect of magnetic field, force, force density and force variation within the effective stroke. Fourth, a suitable cooling structure is designed for the planar motor. Finally, a prototype of the planar motor is constructed and tested. The measured values are in good agreement with results from analysis and FEM.

Index Terms—Analytical model, cooling structure, nanopositioning, planar actuator, planar motor, short stroke.

I. INTRODUCTION

CURRENTLY, multi-DOF positioning system with high accuracy and high frequency response is one of the key technologies in many industrial applications, such as semiconductor lithography, ultra-precision machining, and scanning electron microscope. Conventionally, multi-DOF motion is achieved by stacking multiple linear motors. However, a complex system structure and poor dynamic performance limit the use of this approach for nanopositioning systems. A new approach to multi-DOF positioning, planar motors, has developed rapidly in recent years. Based on their driving principle, planar motors can be classified into reluctance [1]-[4], induction [5]-[7], synchronous [8]-[17], and Lorentz-force [18]-[19] motors. Due to its inherent high resolution and good linearity, the Lorentz-force planar motor is regarded as a superior electromagnetic device for precision compensation in

the nanopositioning systems. Many studies on the structure, performance and control of Lorentz-force planar motors have been published. The analysis of a 3-DOF planar motor for precision positioning in a lithography system and structural improvement made to the design are described in [20]. Based on coupled field analysis, an integrated design for a multi-DOF motor is presented in [21]. A magnetic field model and electromagnetic design method for a novel Lorentz-force-driven planar motor are presented in [19]. An aerostatic 3-DOF planar motor for ultra-precision machining, in which alumina ceramics are used as the structural material for the moving part and the base to achieve low mass and high stiffness, is proposed in [22]. In [18], a 3-DOF coarse-fine dual stage scheme is presented, in which long-stroke motion is achieved with a linear motor and short-stroke motion is achieved with a 3-DOF Lorentz-force-driven planar motor. In [23], a 6-DOF coarse-fine dual stage scheme is described in which the coarse stage uses three linear motors and the fine stage uses a planar motor with four linear active magnetic bearings. Two generations of multi-DOF nanopositioning devices are presented in [24]-[26]. The first device is a Δ stage capable of generating translation over a range of $300\text{ }\mu\text{m}\times 300\text{ }\mu\text{m}$ with a high position resolution. The second device is a Y stage with a large planar travel range of $5\text{ mm}\times 5\text{ mm}$, a better load capacity and a simpler structure. The driving-unit characteristics and 6-DOF dynamic model for a new planar magnetic levitation positioning system are analyzed in [27]. A 3-DOF planar motor combining electromagnetic actuators and a flexure mechanism is modeled and an advanced adaptive sliding-mode controller for the motor is described in [28]. An alternative solution for positioning is provided by piezo-actuated flexure-based mechanisms, which are based on the elastic deformation of a material. Planar actuators using this technology are presented in [29]-[31]. However, the inherent hysteresis, drift nonlinearities and micron-sized stroke present major limitations [32]-[33]. In [34], a compact centimeter-range flexure-based planar precision positioning system is proposed that could be useful for applications in the biomedical sciences. However, it is not suitable for applications such as the nanopositioning wafer stage in semiconductor lithography, which require a large force capacity and the potential for 6-DOF levitation.

The operating principle of the Lorentz-force planar motor is similar to voice coil motor (VCM). Because air-core coils are

Manuscript received April 11, 2014; revised September 4, 2014; accepted October 11, 2014.

Copyright © 2014 IEEE. Personal use of this material is permitted. However, permission to use this material for any other purposes must be obtained from the IEEE by sending a request to pubs-permissions@ieee.org.

The authors are with the Department of Electrical Engineering, Harbin Institute of Technology, Harbin, China (e-mail: antonyamanda@163.com; koubq@hit.edu.cn; zhanghailin0310@gmail.com; jinyinxi2013@126.com).

used, there is no detent force in this type of motor. Ideally, the motor force would be independent of the displacement of the mover. However, the actual motor force is reduced as the mover displacement increases, due to the end magnetic field of the motor. To enable the control system to achieve fast and precise positioning, the force variation with displacement should be kept as low as possible. In this paper, a 3-DOF short-stroke Lorentz-force-driven planar motor using a Halbach permanent magnet array with unequal thickness is studied. The end magnetic field of the motor can be modulated using this magnet configuration.

Additionally, in a multi-DOF actuator integrated by several driving units, the coupling between axes is significant. There is cross influence between the x and y direction because the motions and forces of the driving units are coupled with each other. However, this problem is neglected or simplified in most research. To provide an accurate electromagnetic model for the control system, a complete force expression in which the position coupling and the end force coupling are considered is presented in this paper.

In the existing literature, very little research has been done on cooling systems for 3-DOF Lorentz-force-driven planar motors. When the motor is used in a semiconductor lithography system, the heat gradient will not only cause inaccuracy in the position measuring device but also produce unwanted structural deformation. Therefore, the heat generated by the planar motor must be efficiently transferred. Another contribution of this paper is the cooling system design for the planar motor.

The rest of this paper is organized as follows. The basic configuration of the proposed planar motor is described in Section II. Then, the magnetic field analysis based on the charge model and the image method is presented in Section III. Next, the complete force expression for the planar motor is derived in Section IV. Four typical driving units are compared in Section V, and the superiority of the proposed magnet structure with unequal thickness is demonstrated. The design of the cooling system is presented and the results of a simulation of the cooling effect are provided in Section VI. Finally, a prototype of the Lorentz-force-driven planar motor is fabricated and its static force/torque performances are tested in Section VII. Section VIII concludes the paper.

II. FUNDAMENTAL STRUCTURE

Fig. 1 shows the basic configuration of the 3-DOF planar motor. The planar motor can achieve in-plane motion, i.e., in the x , y and θ_z directions. Out-of-plane motion of the 6-DOF stage, i.e., in the z , θ_x and θ_y directions, can be driven by three gravity compensators (GC), which are not included in this paper. As shown in Fig. 1, the motor consists of three Lorentz-force-driven units, which are equally spaced by 120 degrees around the mass center. In the mechanical structure of the 3-DOF planar motor, three racetrack-shaped coils are embedded into a holding frame. The upper magnets and back irons of the three units are mounted to a large aluminum plate. The lower magnets and back irons are mounted to a small

aluminum plate. The two parts are precisely aligned using three side plates and several dowel pins. To avoid cable disturbance and temperature effects, a moving magnet structure is adopted.

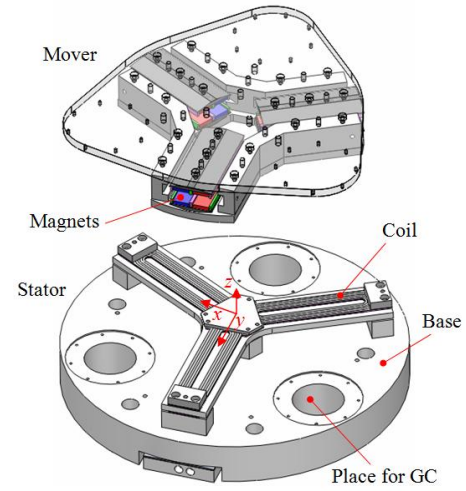


Fig. 1. A 3-D view of the 3-DOF short-stroke Lorentz-force-driven planar motor.

Fig. 2 shows the geometry of the Lorentz driving unit. The mover is a double-sided Halbach magnet array and the stator is a racetrack-shaped coil. Unlike in a conventional Halbach magnet array, the thickness of the magnets with horizontal magnetization is greater than the magnets with vertical magnetization. The objective is to widen the constant-value range of the air-gap magnetic field and reduce the force variation with displacement by modulating the end magnetic field.

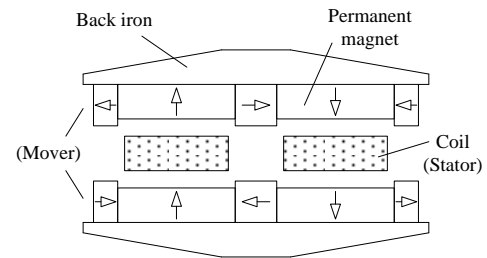


Fig. 2. Lorentz driving unit.

Fig. 3 shows the 3-DOF actuation principle of the planar motor. Assuming that the force in each coil is positive in the clockwise direction, the relation between the motor force and the force produced by each unit can be expressed as

$$\begin{bmatrix} F_x \\ F_y \\ T \end{bmatrix} = \begin{bmatrix} 1 & -\sin 30^\circ & -\sin 30^\circ \\ 0 & \cos 30^\circ & -\cos 30^\circ \\ R & R & R \end{bmatrix} \begin{bmatrix} F_1 \\ F_2 \\ F_3 \end{bmatrix} \quad (1)$$

where R is the moment arm.

III. MAGNETIC FIELD ANALYSIS

For a short-stroke electromagnetic actuator, the equivalent magnetic charge model [35]–[36] is an appropriate model to use to determine the air-gap magnetic field because the end field can be calculated accurately. According to the equivalent magnetic charge model, one magnet with uniform magnetization can be

represented by two charge surfaces whose normal vectors are parallel to the magnetization direction. Fig. 4 shows the equivalent magnetic charge model for magnets with vertical magnetization and horizontal magnetization.

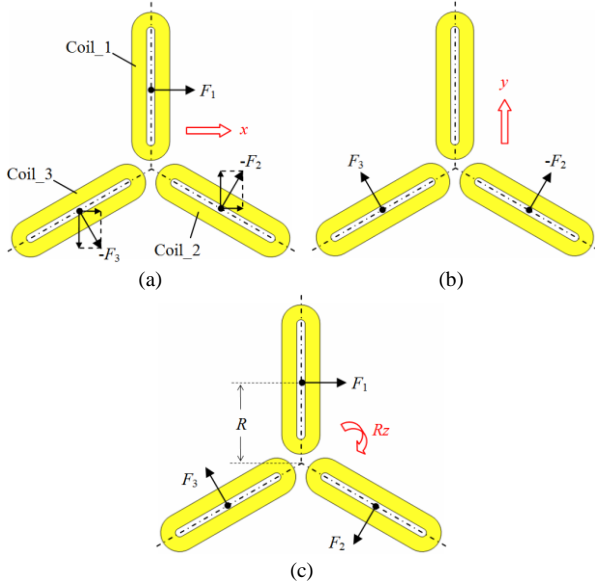


Fig. 3. Analysis of the 3-DOF motion of the motor: (a) translation in the x direction. (b) translation in the y direction. (c) rotation about the z axis.

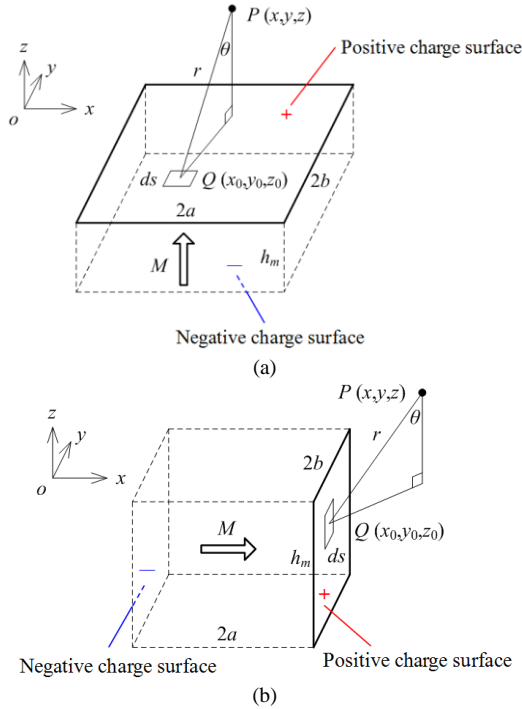


Fig. 4. Equivalent magnetic charge model of a permanent magnet: (a) vertical magnetization (in the z direction). (b) horizontal magnetization (in the x direction).

Based on the charge model, the magnetic flux density generated by a unit-area charge element is expressed as

$$d\vec{B} = \frac{\mu_0 M}{4\pi} \frac{\vec{QP}}{|\vec{QP}|^3} ds \quad (2)$$

where M is the magnetization of the permanent magnet, $Q(x_0, y_0, z_0)$ is the source point of the magnetic charge, and $P(x, y, z)$ is an

arbitrary observation point.

To calculate the horizontal force produced by the planar motor, only the z component of the magnetic field is needed. From Fig. 4(a), the magnetic flux density of the positive charge surface in the xoy plane is

$$B_{z,vertical} = \frac{\mu_0 M}{4\pi} \int_{-b}^b \int_{-a}^a \frac{\cos \theta}{|\vec{QP}|^2} dx_0 dy_0 = \frac{\mu_0 M}{4\pi} \int_{-b}^b \int_{-a}^a \frac{z - z_0}{[(x - x_0)^2 + (y - y_0)^2 + (z - z_0)^2]^{3/2}} dx_0 dy_0 \quad (3)$$

Through double integration and derivation, equation (3) can be analytically represented by four arctangent functions of the magnet dimensions. When the flux density of the negative charge surface is calculated, only the sign of the expression is reversed.

Assuming that the geometric center of the magnet coincides with the coordinate origin, the analytical expression for the z component of the magnetic flux density of the magnet with vertical magnetization can be derived as

$$B_{z,vertical} = \frac{\mu_0 M}{4\pi} \cdot \{ \zeta(a - x, b - y, z - h_m/2) + \zeta(a - x, b + y, z - h_m/2) + \zeta(a + x, b - y, z - h_m/2) + \zeta(a + x, b + y, z - h_m/2) - \zeta(a - x, b - y, z + h_m/2) - \zeta(a - x, b + y, z + h_m/2) - \zeta(a + x, b - y, z + h_m/2) - \zeta(a + x, b + y, z + h_m/2) \} \quad (4)$$

where $2a$, $2b$ and h_m are the length, width, and thickness of the magnet, respectively, and the function ζ is

$$\zeta(\zeta_1, \zeta_2, \zeta_3) = \arctg \frac{\zeta_1 \cdot \zeta_2}{\zeta_3 \cdot \sqrt{\zeta_1^2 + \zeta_2^2 + \zeta_3^2}} \quad (5)$$

From Fig. 4(b), the z component of the magnetic flux density of the positive charge surface in the yoz plane is

$$B_{z,horizontal} = \frac{\mu_0 M}{4\pi} \int_{-b}^b \int_{-h_m/2}^{h_m/2} \frac{\cos \theta}{|\vec{QP}|^2} dz_0 dy_0 = \frac{\mu_0 M}{4\pi} \int_{-b}^b \int_{-h_m/2}^{h_m/2} \frac{z - z_0}{[(x - x_0)^2 + (y - y_0)^2 + (z - z_0)^2]^{3/2}} dz_0 dy_0 \quad (6)$$

Similarly, equation (7) can be written using four logarithmic functions. The analytical expression for the z component of the magnetic flux density of the magnet with horizontal magnetization can then be derived as

$$B_{z,horizontal} = \frac{\mu_0 M}{4\pi} \cdot \{ \Gamma(x - a, y - b, z) - \Gamma(x - a, y + b, z) - \Gamma(x + a, y - b, z) + \Gamma(x + a, y + b, z) \} \quad (7)$$

where

$$\Gamma(r_1, r_2, r_3) = \ln \frac{\sqrt{r_1^2 + r_2^2 + (r_3 - z_0)^2} - r_2}{\sqrt{r_1^2 + r_2^2 + (r_3 - z_0)^2} + r_2} \Big|_{z_0 = h_m/2}^{z_0 = -h_m/2} \quad (8)$$

Additionally, the influence of the ferromagnetic boundary must be taken into account using the image method [37]. The actual magnetic field is the superposition of the original charge field and the image charge field. For two parallel ferromagnetic boundaries, there are infinite image charge surfaces. Fig. 5 shows the distribution of the image charge surfaces.

As shown in Fig. 2, there are ten magnets in the mover of each

Lorentz-force-driven unit. Taking the corresponding upper and lower magnets as one pair, the final air-gap magnetic field can be expressed as

$$B_z = \sum_{m=1}^2 [B_{zm,vertical} + \sum_{k=1}^{\infty} B_{zmk,vertical,image}] + \sum_{n=1}^3 [B_{zn,horizontal} + \sum_{l=1}^{\infty} B_{znl,horizontal,image}] \quad (9)$$

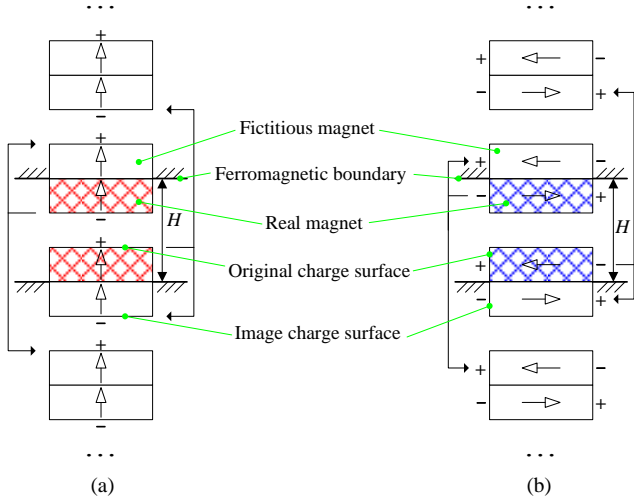


Fig. 5. Concept of the image method: (a) vertical magnetization (in the z direction). (b) horizontal magnetization (in the x direction).

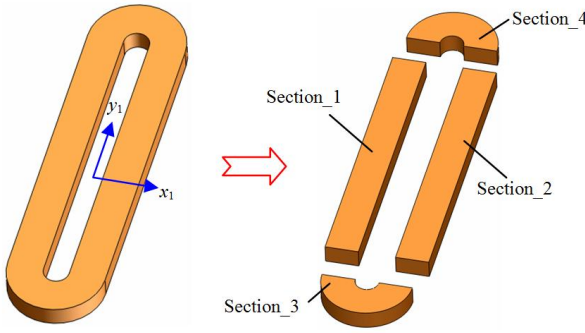


Fig. 6. Diagram showing the coil sections.

IV. FORCE EXPRESSION

Using the Lorentz force law, the force can be calculated after the analytical expression for the magnetic field has been obtained. Note that the planar motor is a multi-DOF motor, and electromagnetic coupling is inevitable between the Lorentz driving units. When the performance of a linear motor is analyzed, some secondary factors are always neglected. For example, it is assumed that the end sections of the windings do not contribute to the motor force. However, the end section of a coil could provide additional force in other directions in the planar motor. In a precision positioning system, the additional force cannot be ignored. Therefore, the end sections of the coils need to be considered for obtaining the accurate multi-DOF forces of planar motor.

The proposed planar motor is composed of three Lorentz driving units. Before calculating the motor force, the unit force must be calculated. Fig. 6 shows a diagram of the coil sections.

The coordinate origin is located at the geometric center of the coil. The x_1 axis is parallel to the direction of the main force, and the y_1 axis is parallel to the straight section of the coil. As shown in Fig. 6, each coil can be divided into four sections. Section_1 and section_2 are the straight parts. Section_3 and section_4 are the end parts. In the straight parts, the current has only a y component. In the end parts, the current has both x and y components. Therefore, the unit force can be expressed as

$$\begin{cases} F_{x,unit} = \int_{V_1+V_2+V_3+V_4} B_z \cdot J_y \cdot dv \\ F_{y,unit} = \int_{V_3+V_4} B_z \cdot J_x \cdot dv \end{cases} \quad (10)$$

where V_1 - V_4 are the volume of coil sections 1-4, respectively, and J_x and J_y are the x and y components of the current density, respectively.

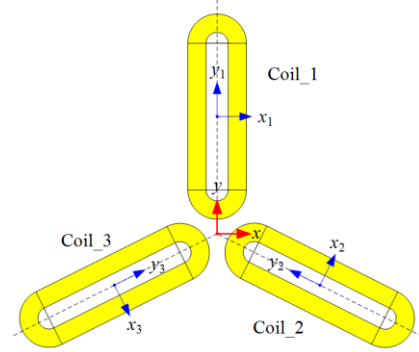


Fig. 7. Definition of the coordinate systems for the planar motor.

Fig. 7 shows the definition of the coordinate systems for the planar motor. The global coordinate system is located in the center of the three coils, and there is a local coordinate system for each coil. When the motor moves, the relative displacement of coil_1 is the same as the global displacement of the motor because the local coordinate system of coil_1 is parallel to the global coordinate system. However, this is not true for coil_2 and coil_3. Therefore, the relative displacements of coil_2 and coil_3 need to be derived based on geometrical relationships. The unit forces of coil_2 and coil_3 can then be calculated in their local coordinate systems. Finally, the motor force is determined from the projections of the three unit forces in the global coordinate system.

When the motor moves in the x direction, the relative displacements of coil_2 and coil_3 in the x_2y_2 and x_3y_3 coordinate systems, respectively, are

$$\begin{cases} dx_2 = dx_3 = dx \cdot \sin 30^\circ \\ dy_2 = -dy_3 = -dx \cdot \cos 30^\circ \end{cases} \quad (11)$$

where dx is the motor displacement in the x direction.

When the motor moves in the y direction, the relative displacements of coil_2 and coil_3 in the x_2y_2 and x_3y_3 coordinate systems, respectively, are

$$\begin{cases} dx_2 = -dx_3 = dy \cdot \cos 30^\circ \\ dy_2 = dy_3 = dy \cdot \sin 30^\circ \end{cases} \quad (12)$$

where dy is the motor displacement in the y direction.

The contribution of coil_2 to the motor force is expressed as

TABLE I
THE INITIAL DIMENSIONS OF THE FOUR TYPICAL DRIVING UNITS

| Symbol | A | B | C | D | Unit |
|----------|-----|-----|-----|-----|------|
| h_{m1} | 4.5 | 4.5 | 4.5 | 4.5 | mm |
| h_{m2} | - | 4.5 | 4.5 | 6.5 | mm |
| h_{m3} | - | - | 4.5 | 6.5 | mm |
| w_{m1} | 20 | 20 | 20 | 20 | mm |
| w_{m2} | - | 4 | 4 | 4 | mm |
| w_{m3} | - | - | 2.5 | 2.5 | mm |
| l_m | 115 | 115 | 115 | 115 | mm |
| h_c | 8 | 8 | 8 | 8 | mm |
| w_c | 14 | 14 | 14 | 14 | mm |
| g | 3.8 | 3.8 | 3.8 | 3.8 | mm |

$$\begin{cases} F_x = F_{2x} \sin 30^\circ - F_{2y} \cos 30^\circ \\ F_y = F_{2x} \cos 30^\circ + F_{2y} \sin 30^\circ \end{cases} \quad (13)$$

The contribution of coil_3 to the motor force is expressed as

$$\begin{cases} F_x = F_{3x} \sin 30^\circ + F_{3y} \cos 30^\circ \\ F_y = -F_{3x} \cos 30^\circ + F_{3y} \sin 30^\circ \end{cases} \quad (14)$$

In sum, the final force expression for the planar motor is

$$\begin{cases} F_x = F_{1x} + F_{2x} \sin 30^\circ - F_{2y} \cos 30^\circ \\ \quad + F_{3x} \sin 30^\circ + F_{3y} \cos 30^\circ \\ F_y = F_{1y} + F_{2x} \cos 30^\circ + F_{2y} \sin 30^\circ \\ \quad - F_{3x} \cos 30^\circ + F_{3y} \sin 30^\circ \end{cases} \quad (15)$$

On account of the end magnetic field, the end force is less than the center force. The force variation is defined as

$$\Delta F = \frac{F_{center} - F_{end}}{F_{center}} \times 100\% \quad (16)$$

As the mover rotates about the z axis, the torque of the planar motor is expressed as

$$T = 3 \times F \cdot R \quad (17)$$

V. COMPARISON OF TYPICAL DRIVING UNITS

To decrease the force variation within the effective stroke of the planar motor, a Lorentz-force-driven unit with unequal magnet thickness is adopted. Based on the analytical model derived above, we compare four types of Lorentz-force-driven units in this section. Fig. 8 shows the configurations of four planar motor driving units. The first configuration consists only of magnets with vertical magnetization. The second configuration adds center magnets with horizontal magnetization. The third configuration adds end magnets. The last configuration uses a Halbach array with unequal thickness as proposed in this paper. The dimensions of the four units are shown in Table I, in which the parameter l_m is the length of magnet. The magnets are N48H whose remanence is 1.387T. The relative permeability is 1.026.

Fig. 9 shows the central air-gap magnetic field for the four planar motor driving units. From Fig. 9, we can see that increasing the thickness of the magnet with horizontal magnetization improves the amplitude of the magnetic flux density. Additionally, the increase in the end magnetic field is

greater than in the center magnetic field. This produces a magnetic field with a more rectangular shape, thereby decreasing the force variation.

Fig. 10 shows the force-displacement curves for the four planar motor driving units. The presence of the center magnet with horizontal magnetization effectively increases the unit force. Compared with unit a, the force amplitude of unit b is increased by 3.3%. When the end magnets are added, the force increases further. The increase is relatively small because the end magnets is relatively small. However, the unit force is greatly increased when the thickness of the center magnet and end magnet are increased.

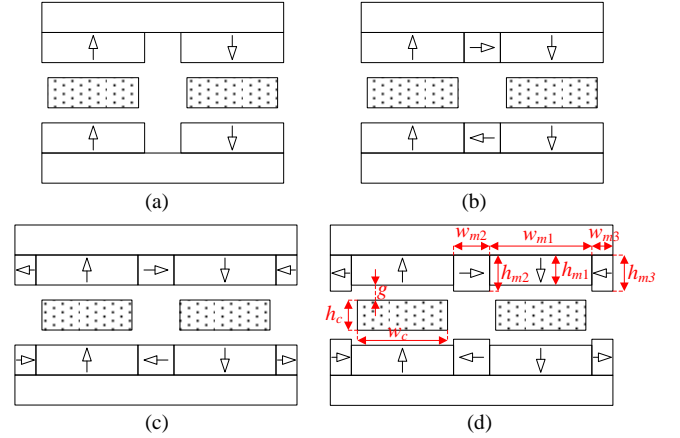


Fig. 8. Typical Lorentz driving units. (a) unit a: conventional type. (b) unit b: a magnet is added with horizontal magnetization. (c) unit c: a Halbach array with equal thickness. (d) unit d: a Halbach array with unequal thickness.

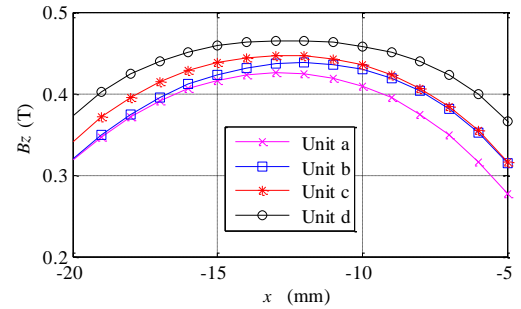


Fig. 9. The central air-gap magnetic field for the four driving units.

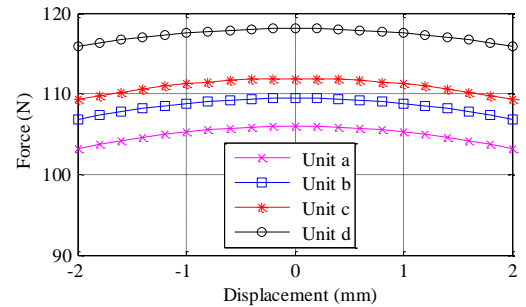


Fig. 10. Force-displacement curves for the four driving units.

Fig. 11 shows the comparison results of the four driving units. Compared with the conventional Halbach array, the force amplitude of the Halbach array with unequal thickness is increased by 5.5%. The force densities of unit a, b and d are basically the same. However, the force variation within ± 2 mm

for unit d is decreased by 29%, which is a superiority in the precision positioning system. In sum, by enhancing the end magnetic field, the proposed driving unit not only increases the force amplitude but also decreases the force variation. In addition, the force density of the proposed driving unit is greater than the conventional Halbach array, but it is at the same level as unit a and unit b.

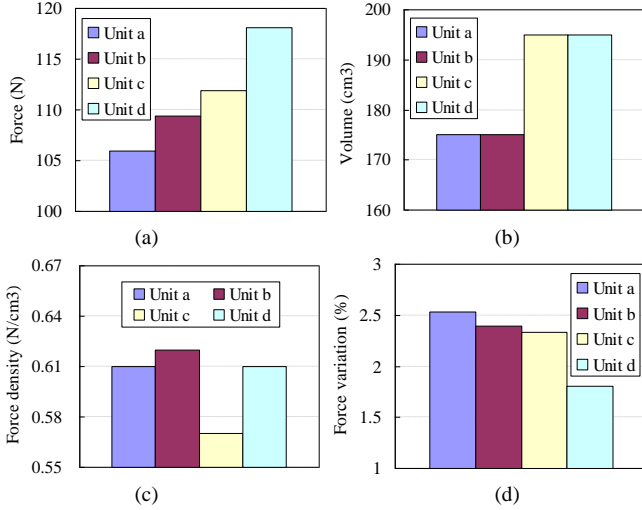


Fig. 11. Comparison of results from the four driving units. (a) force amplitude. (b) volume. (c) force density. (d) force variation within ± 2 mm.

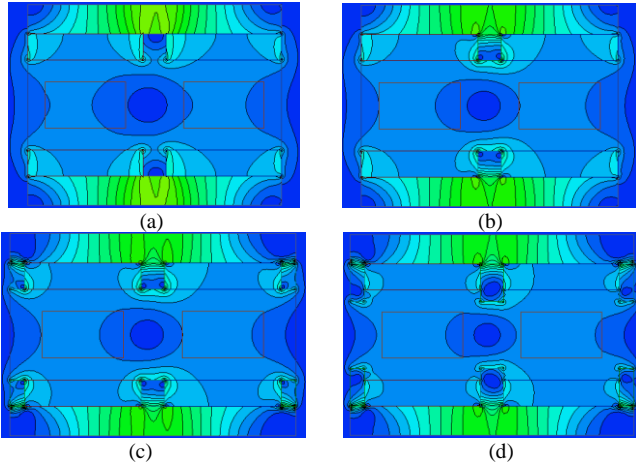


Fig. 12. Magnetic flux density distribution and contour lines for the four driving units. (a) unit a: conventional type. (b) unit b: a magnet is added with horizontal magnetization. (c) unit c: a Halbach array with equal thickness. (d) unit d: a Halbach array with unequal thickness.

Fig. 12 shows the magnetic flux density distribution and contour lines for the four driving units. Due to the end magnetic field of the mover magnets, the magnetic flux density at the ends of the coil cross section is less than in the center region. There is a circular "hole" in the field between the two coil cross sections. The flux density decreases sharply from the outer loop to the inner loop. Fig. 12(b) and 12(c) show that the use of center and end magnets with horizontal magnetization can partially modulate the end magnetic field. In Fig. 12(d), we can see that the increase in the magnet thickness further improves the uniformity of the air-gap magnetic field. When the Halbach array with unequal thickness is used, the size of the circular

"hole" is reduced and the amplitude of the magnetic field in the coil region is more uniform than in the other three units.

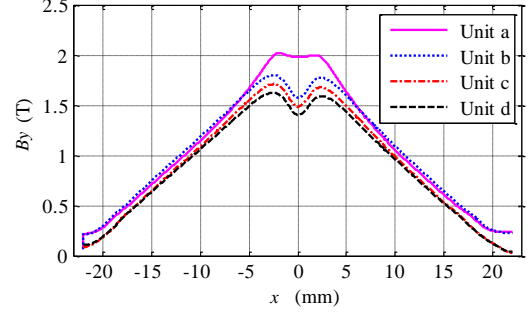


Fig. 13. The magnetic field distribution in the center line of the back iron.

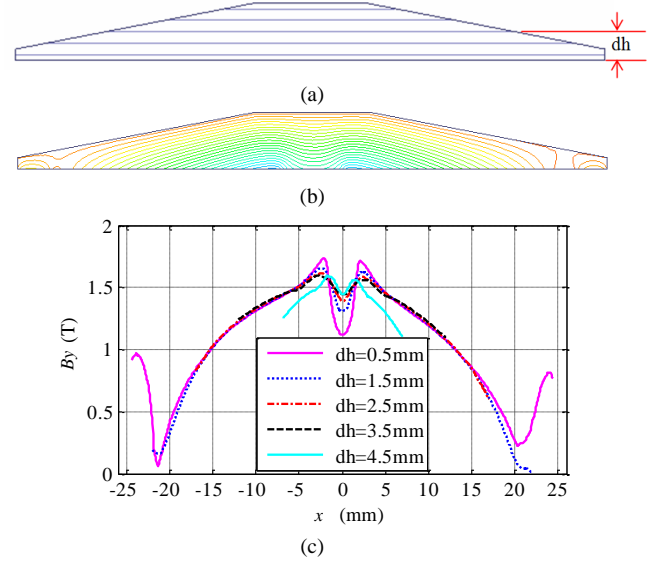


Fig. 14. The trapezoidal back iron of unit d for lightweight design. (a) structural diagram with five auxiliary lines. (b) lines of magnetic flux calculating using the finite element method. (c) magnetic flux density curves, where dh is the distance between the auxiliary line and the lower side of the back iron.

Fig. 13 compares the magnetic field distribution at the center line of the back iron for the four driving units. The maximum value of the magnetic field in the back iron occurs in the middle and the magnetic field decreases linearly as the x position increases. Therefore, the shape of the back iron can be optimized to reduce the weight of the mover. Besides, the magnetic field in the back iron is lowest for unit d, which is good for decreasing the thickness of the back iron and the mover mass. In Fig. 13, the amplitude of the magnetic flux density for unit a is 2.02 T which is decreased to 1.62 T in the unit d.

Fig. 14(a) shows the trapezoidal back iron of unit d, which is designed for light weight [38]–[39]. Compared with the conventional rectangular shape, the mass of the back iron is reduced by 31.8%. The magnetic field lines for the trapezoidal back iron are shown in Fig. 14(b). Fig. 14(c) shows the magnetic flux density along the five auxiliary lines in the trapezoidal back iron. It can be seen that the amplitude of the field is 1.73 T, which is essentially the same as before. Therefore, the mass of the back iron can be reduced without affecting the amplitude of the magnetic flux density.

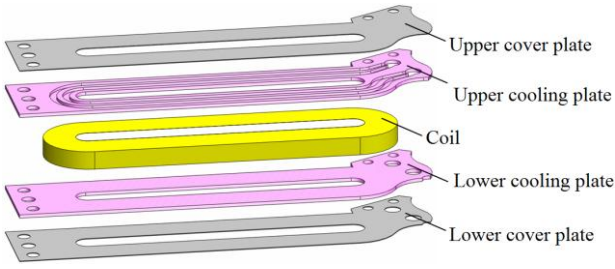


Fig. 15. Configuration of the double-sided cooling structure for one coil.

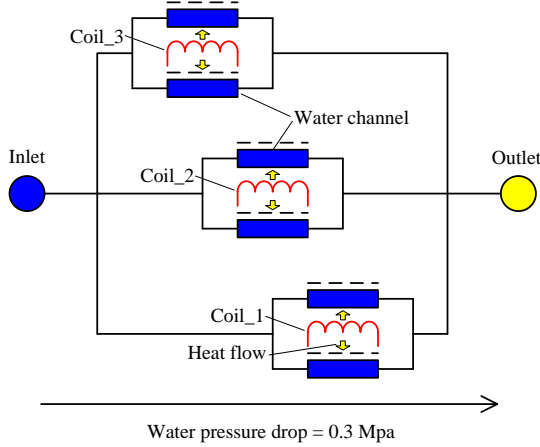


Fig. 16. Schematic diagram of the cooling system.

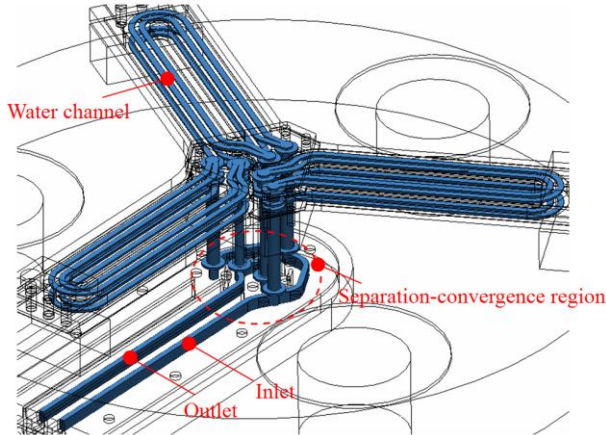


Fig. 17. The flow path of the cooling liquid.

VI. DESIGN OF THE COOLING SYSTEM

In precision positioning applications, an environmental temperature gradient reduces the measurement accuracy of the laser interferometer. A temperature rise also causes undesired structural distortion. These factors will eventually lead to the loss of the system positioning accuracy. Therefore, a cooling system is an essential component for a planar motor used in precision positioning applications.

There are three coils in the proposed planar motor, and the coils are configured in a Y-shaped arrangement. Consequently, the volume will be increased unnecessarily if the three coils are located in the same closed cooling box. In this paper, an independent cooling structure is adopted for each coil. Fig. 15 shows the configuration of the double-sided cooling structure of one coil. There are two channels for the cooling liquid in the

cooling plate and the cooling plates are glued to the coils with epoxy resin. To decrease the flow resistance, the three branches of the cooling system are connected in parallel. The three branches follow the principle of "first-in last-out" for the average flow path. A schematic diagram of the cooling system is shown in Fig. 16. The flow path of the cooling liquid is shown in Fig. 17.

The commercial finite element software ANSYS is used to analyze the static temperature field of the stator part of the planar motor. The heat source and the cooling boundary condition must be calculated first.

The internal heat generation of the coil is expressed as

$$S = \frac{P_{Cu}}{V_C} \quad (18)$$

where P_{Cu} is the copper loss from the coil and V_C is the volume of the coil.

The convective heat transfer coefficient of the cooling channel is expressed as

$$h = \frac{\lambda_f}{d_e} Nu_f \quad (19)$$

where λ_f is the thermal conductivity of the fluid, d_e is the equivalent diameter of the water channel and Nu_f is the Nusselt number.

The equivalent diameter of a non-circular cooling channel is

$$d_e = \frac{4A_e}{P} \quad (20)$$

where A_e is the cross-sectional area of the cooling channel and P is the wet perimeter.

In (19), the Nusselt number is calculated using the Dittus-Boelter equation, which is expressed as

$$Nu_f = 0.023 Re_f^{0.8} Pr_f^{0.4} \quad (21)$$

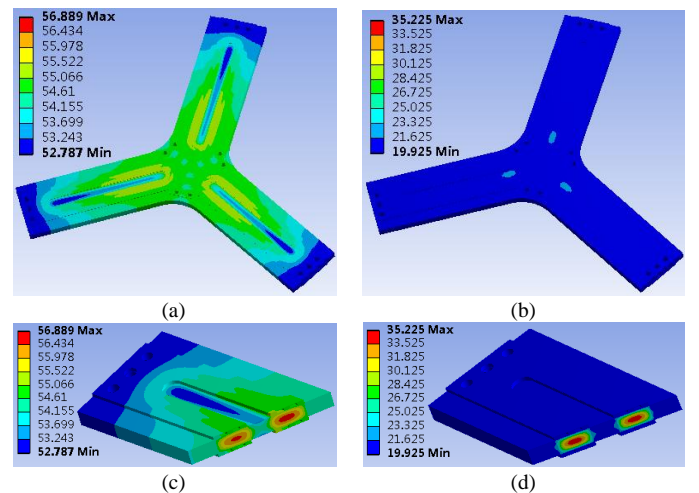


Fig. 18. Temperature distribution in the stator part of the planar motor. (a) natural cooling condition at $J=5$ A/mm². (b) water cooling condition at $J=15$ A/mm². (c) slice plane in natural cooling condition at $J=5$ A/mm². (d) slice plane in water cooling condition at $J=15$ A/mm².

Fig. 18 shows the temperature distribution in the stator part of the planar motor. In Fig. 18(a), the coils are under natural cooling condition, and the current density is selected as 5 A/mm². In Fig. 18(b), the coils are under water cooling condition, and the current density is increased to 15 A/mm². The

maximum temperature reaches 56.9 °C without water cooling at a low current density. In contrast, the temperature rise of the stator part is low with water cooling, even at a high current density. Therefore, the proposed cooling structure effectively reduces the heat transmission from the coils to the environment. On the other hand, the force and the force density of the planar motor can be significantly improved due to the increase in the current density.

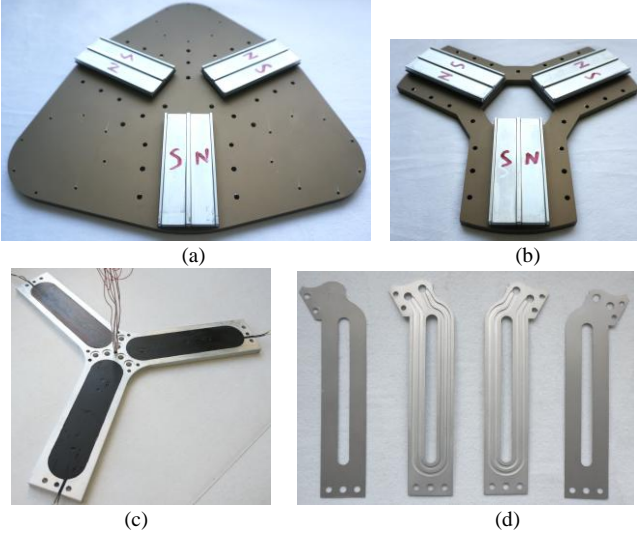


Fig. 19. Parts of the prototype for the short stroke lorentz-force-driven planar motor using a Halbach permanent magnet array with unequal thickness. (a) the upper mover. (b) the lower mover. (c) coils and holding frame. (d) the cooling plate.

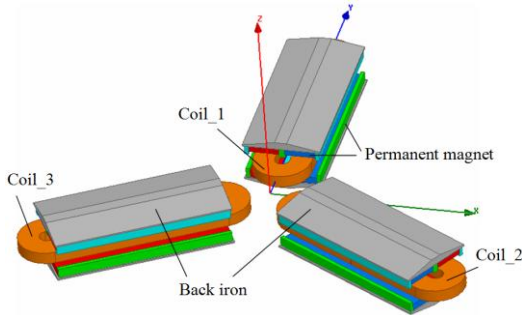


Fig. 20. The 3-D finite element model of the short-stroke lorentz-force-driven planar motor.

VII. SIMULATION AND EXPERIMENT

Based on the above analysis, a prototype of the 3-DOF short-stroke Lorentz-force-driven planar motor using a Halbach permanent magnet array with unequal thickness is designed and constructed. The main components are shown in Fig. 19. The parameters of the prototype are the same to unit d, shown in Table I.

Fig. 20 shows the 3-D finite element model of the planar motor for the verification of the magnetic field and force. Fig. 21(a) shows the analytical magnetic field distribution of the driving unit. The maximum value of B_z is 0.461T. Fig. 21(b) shows the field deviation between analysis and FEM. The maximum difference between the magnetic flux density calculated from the analytical model and FEM is only 0.013 T, which is approximately 2.8% of the amplitude of the air-gap magnetic field.

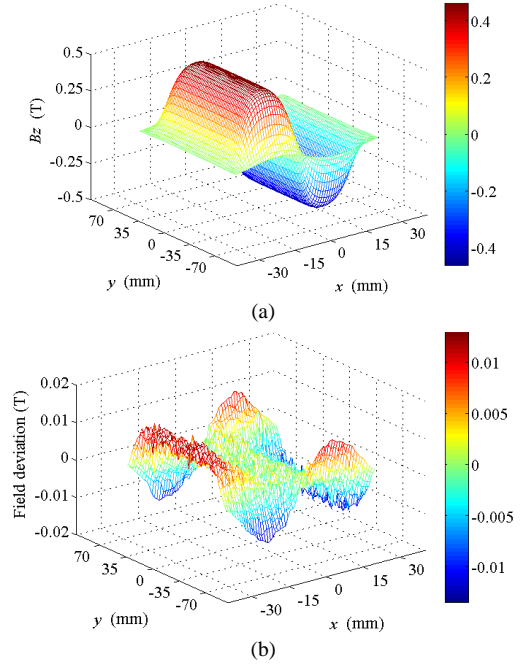


Fig. 21. Air-gap magnetic field distribution of the driving unit. (a) analytical results. (b) comparison between the analytical results and the FEM results.

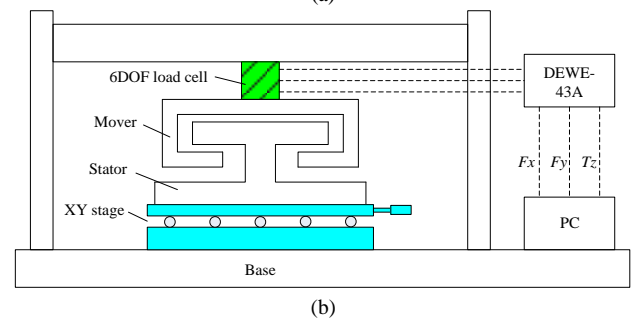
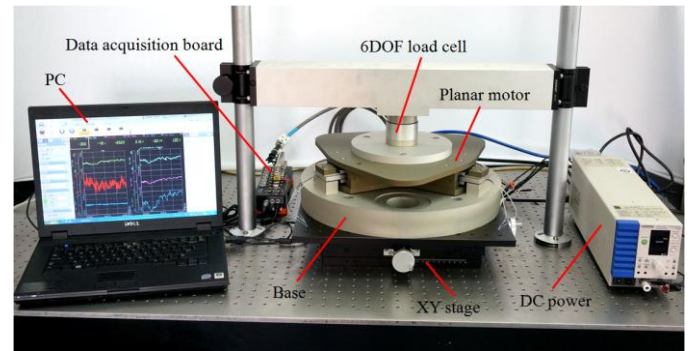


Fig. 22. The static force/torque testing platform for the planar motor. (a) picture. (b) schematic diagram.

Fig. 22 shows the static force/torque testing platform for the planar motor. To evaluate the force and torque characteristics of the prototype, a 6-DOF load cell (AD2.5D, AMTI) is used. The multi-channel data acquisition board selected is the DEWE-43A. The mover of the motor is fixed on a supporting beam through the load cell. The stator of the motor is fastened onto an XY stage. The relative position between the stator and the mover in the xoy plane can be changed by the XY stage. The manual adjustment resolution of the XY stage is 0.02 mm. The other components of the testing platform include a DC power source

(PWR400L, KIKUSUI), a water cooling machine and a computer.

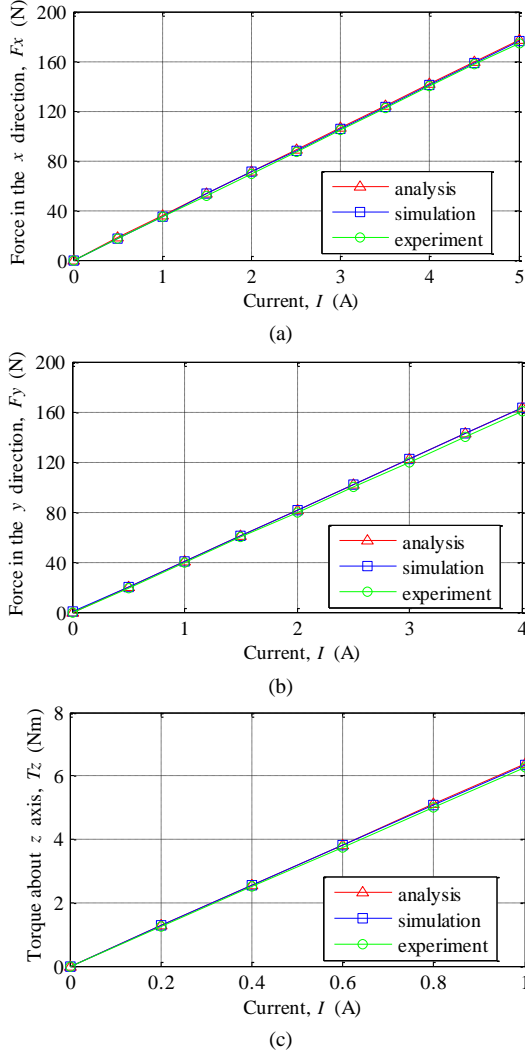


Fig. 23. Force and torque as a function of the current. (a) force in the x direction. (b) force in the y direction. (c) torque about the z axis.

Fig. 23 shows the force-current and torque-current relationships. In Fig. 23(a), the abscissa represents the current in coil_1, and the current in coil_2 and coil_3 is one-half. When $I_1=5A$, the force F_x from analysis, simulation and experiment are 177.1N, 176.7N and 174.8N, respectively. In Fig. 23(b), the abscissa represents the current in coil_2 and coil_3, and the current in coil_1 is zero. When $I_2=4A$, the force F_y from analysis, simulation and experiment are 163.6N, 163.3N and 160.4N, respectively. In Fig. 23(c), the current in the three coils is the same. When the current is 1A, the torque T_z from analysis, simulation and experiment are 6.376Nm, 6.360Nm and 6.272Nm, respectively. From Fig. 23, the force (F_x , F_y) and torque (T_z) both increase linearly with the current. In addition, the analytical results match well with the simulation results. The error between analysis and simulation is less than 0.3%. The experiment results are slightly lower than the simulation ones. The differences are mainly caused by the magnetization error of magnets, manufacturing tolerances and installation tolerances.

However, the maximum error between simulation and experiment is only about 1.8%, which is within an acceptable range.

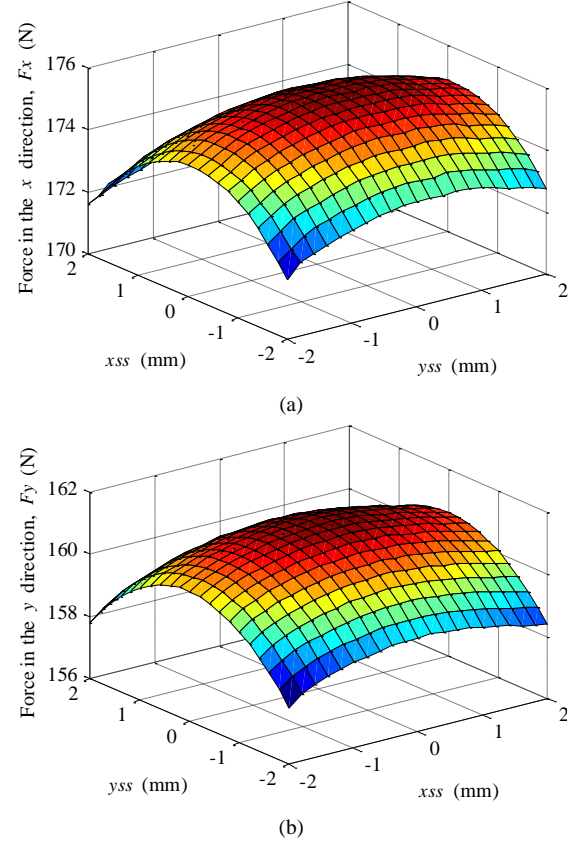


Fig. 24. The measured force distribution within the effective stroke. (a) force in the x direction ($I_1=5A$, $I_2=I_3=2.5A$, $J_1=15A/mm^2$, $J_2=J_3=7.5A/mm^2$). (b) force in the y direction ($I_1=0$, $I_2=I_3=4A$, $J_2=J_3=12A/mm^2$).

Fig. 24 shows the force distribution in the xoy workspace. In Fig. 24(a), the maximum force in the x direction is 175.52N. The force variation when $x_{ss}=[-2.0, 2.0]$ ($y_{ss}=0$) is 1.58%. The force variation when $x_{ss}=[-1.0, 1.0]$ ($y_{ss}=0$) is 0.44%. The force constant of the planar motor in the x direction is 35.1N/A. In Fig. 24(b), the maximum force in the y direction is 161.28N. The force variation when $y_{ss}=[-2.0, 2.0]$ ($x_{ss}=0$) is 1.39%. The force variation when $y_{ss}=[-1.0, 1.0]$ ($x_{ss}=0$) is 0.34%. The force constant of the planar motor in the y direction is 40.32N/A.

VIII. CONCLUSION

In this paper, we have designed and analyzed a 3-DOF short-stroke Lorentz-force-driven planar motor, which serves as the precision compensation actuator in a nanopositioning system. To enable the precise control of 3-DOF motion, accurate expressions are derived for the magnetic field and force. To decrease the inherent force variation with displacement, an improved Halbach permanent magnet array with unequal thickness is adopted. By comparison, the proposed secondary magnet array improves the smoothness of the end field without affecting the output force and the mechanical installation. Moreover, a cooling system is designed for the 3-DOF Lorentz-force-driven planar motor that transfers the

majority of the heat from the three coils through the cooling plates. The low heat dissipation of the planar motor makes it suitable for semiconductor lithography applications. To demonstrate the actual performance of the planar motor, static experiments are conducted. The results of the analysis, simulation and experiment show good agreement with each other.

In summary, the main contribution of this paper is the analysis and design of a 3-DOF Lorentz-force-driven planar motor for high precision applications, which includes the electromagnetic field and the temperature field. Based on the analysis and experiment, the proposed planar motor has high force/torque linearity and low force variation. Additionally, the effective cooling structure not only increases the force density but also decrease the surface temperature rise, which are both the crucial factors for the wafer stage. The high force ensures the stage acceleration and the low temperature rise avoids the influence from the motor to the measurement environment for laser interferometer. In future work, a control system will be developed for the 3-DOF planar motor. Additionally, key problems such as dynamics analysis and optimization will be addressed.

REFERENCES

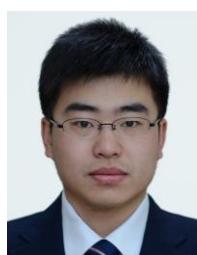
- [1] E. R. Pelta, "Two-axis Sawyer motor for motion systems," *IEEE Contr. Syst. Mag.*, vol. 7, no. 5, pp. 20–24, Oct. 1987.
- [2] J. F. Pan, N. C. Cheung, W. C. Gan, and S. W. Zhao, "A novel planar switched reluctance motor for industrial applications," *IEEE Trans. Magn.*, vol. 42, no. 10, pp. 2836–2839, May. 2006.
- [3] J. Pan, N. Cheung, and J. Yang, "High-precision position control of a novel planar switched reluctance motor," *IEEE Trans. Ind. Electron.*, vol. 52, no. 6, pp. 1644–1652, Dec. 2005.
- [4] J. F. Pan, F. J. Meng, and N. C. Cheung, "Core loss analysis for the planar switched reluctance motor," *IEEE Trans. Magn.*, vol. 20, no. 2, pp. 7020104, Feb. 2014.
- [5] N. Fujii and M. Fujitake, "Two-dimensional drive characteristics by circular-shaped motor," *IEEE Trans. Ind. Appl.*, vol. 35, no. 4, pp. 803–809, Jul./Aug. 1999.
- [6] P. Dittich and D. Radeck, "3-Dof planar induction motor," in *Proc. IEEE Electro/information technology Conf.*, May. 7–10, 2006, pp. 81–86.
- [7] A. Filho and N. Filho, "Analysis of an induction planar actuator," in *Proc. XIX ICEM*, 2010, pp. 1–6.
- [8] W. J. Kim and D. L. Trumper, "High-precision magnetic levitation stage for photolithography," *Precision Eng.*, vol. 22, no. 2, pp. 66–77, Apr. 1998.
- [9] J. M. M. Rovers, J. W. Jansen, J. C. Compter, and E. A. Lomonova, "Analysis method of the dynamic force and torque distribution in the magnet array of a commutated magnetically levitated planar actuator," *IEEE Trans. Ind. Electron.*, vol. 59, no. 5, pp. 2157–2166, May. 2012.
- [10] J. W. Jansen, C. M. M. van Lierop, E. A. Lomonova, and A. J. A. Vandenput, "Modeling of magnetically levitated planar actuators with moving magnets," *IEEE Trans. Magn.*, vol. 43, no. 1, pp. 15–25, Jan. 2007.
- [11] J. de Boeij, E. Lomonova, and A. Vandenput, "Modeling ironless permanent-magnet planar actuator structures," *IEEE Trans. Magn.*, vol. 42, no. 8, pp. 2009–2016, Aug. 2006.
- [12] H. S. Cho and H. K. Jung, "Analysis and design of synchronous permanent-magnet planar motors," *IEEE Trans. Energy Convers.*, vol. 17, no. 4, pp. 492–499, Dec. 2002.
- [13] J. Y. Cao, Y. Zhu, W. C. Gan, J. S. Wang, W. S. Yin, and G. H. Duan, "A novel synchronous permanent magnet planar motor and its model for control applications," *IEEE Trans. Magn.*, vol. 41, no. 6, pp. 2156–2163, Jun. 2005.
- [14] L. Zhang, B. Kou, F. Xing, and H. Zhang, "Analysis and comparison of two two-dimensional Halbach permanent magnet arrays for magnetically levitated planar motor," *Journal of Applied Physics.*, vol. 115, no. 17, pp. 17E704, May. 2014.
- [15] J. Peng and Y. Zhou, "Modeling and analysis of a new 2-D Halbach array for magnetically levitated planar motor," *IEEE Trans. Magn.*, vol. 49, no. 1, pp. 618–627, Jan. 2013.
- [16] J. Peng, Y. Zhou, and G. Liu, "Calculation of a new real-time control model for the magnetically levitated ironless planar motor," *IEEE Trans. Magn.*, vol. 49, no. 4, pp. 1416–1422, Apr. 2013.
- [17] J. M. M. Rovers, J. W. Jansen, and E. A. Lomonova, "Multiphysical analysis of moving-magnet planar motor topologies," *IEEE Trans. Magn.*, vol. 49, no. 12, pp. 5730–5741, Dec. 2013.
- [18] J. Lei, X. Luo, X. Chen, and T. Yan, "Modeling and analysis of a 3-DOF Lorentz-force-driven planar motion stage for nanopositioning," *Mechatronics.*, vol. 20, no. 5, pp. 553–565, Aug. 2010.
- [19] B. Kou, H. Zhang, and L. Li, "Analysis and design of a novel 3-DOF Lorentz-force-driven DC planar motor," *IEEE Trans. Magn.*, vol. 47, no. 8, pp. 2118–2126, Aug. 2011.
- [20] D. J. Lee, K. N. Lee, N. C. Park, etc., "Development of 3-axis nano stage for precision positioning in lithography system," in *Proc. International Conference on Mechatronics & Automation*, 2005, pp. 1598–1603.
- [21] D. J. Lee and J. H. Kim, "Integrated design method of multi-axis VCM actuators based on coupled-field-analysis of electro-magnetics and structure," *IEEE Trans. Magn.*, vol. 45, no. 5, pp. 2340–2343, May. 2009.
- [22] H. Shinno, H. Yoshioka, and K. Taniguchi, "A newly developed linear motor-driven aerostatic X-Y planar motion table system for nano-machining," *Annals of the CIRP.*, vol. 56, no. 1, pp. 369–372, 2007.
- [23] Y. M. Choi and D. G. Gweon, "A high-precision dual-servo stage using Halbach linear active magnetic bearings," *IEEE/ASME Trans. Mechatronics.*, vol. 16, no. 5, pp. 925–931, Oct. 2011.
- [24] S. Verma, W. J. Kim, and J. Gu, "Six-axis nanopositioning device with precision magnetic levitation technology," *IEEE/ASME Trans. Mechatronics.*, vol. 9, no. 2, pp. 384–391, Jun. 2004.
- [25] S. Verma, H. Shakir, and W. J. Kim, "Novel electromagnetic actuation scheme for multiaxis nanopositioning," *IEEE Trans. Magn.*, vol. 42, no. 8, pp. 2052–2062, Aug. 2006.
- [26] W. J. Kim, S. Verma, and H. Shakir, "Design and precision construction of novel magnetic-levitation-based multi-axis nanoscale positioning systems," *Precision Eng.*, vol. 31, no. 4, pp. 337–350, Oct. 2007.
- [27] M. Y. Chen, T. B. Lin, S. K. Hung, and L. C. Fu, "Design and experiment of a macro-micro planar maglev positioning system," *IEEE Trans. Ind. Electron.*, vol. 59, no. 11, pp. 4128–4139, Nov. 2012.
- [28] M. Y. Chen, H. H. Huang, and S. K. Hung, "A new design of a submicropositioner utilizing electromagnetic actuators and flexure mechanism," *IEEE Trans. Ind. Electron.*, vol. 57, no. 1, pp. 96–106, Jan. 2010.
- [29] Y. Li and Q. Xu, "Design and analysis of a totally decoupled flexurebased XY parallel micromanipulator," *IEEE Trans. Robot.*, vol. 25, no. 3, pp. 645–657, Jun. 2009.
- [30] Y. Li and Q. Xu, "A novel piezoactuated XY stage with parallel, decoupled, and stacked flexure structure for micro-/nanopositioning," *IEEE Trans. Ind. Electron.*, vol. 58, no. 8, pp. 3601–3615, Aug. 2011.
- [31] Y. K. Yong, S. Aphale, and S. O. R. Moheimani, "Design, identification and control of a flexure-based XY stage for fast nanoscale positioning," *IEEE Trans. Nanotechnol.*, vol. 8, no. 1, pp. 46–54, Jan. 2009.
- [32] C. M. Wen and M. Y. Cheng, "Development of a recurrent fuzzy CMAC with adjustable input space quantization and self-tuning learning rate for control of a dual-axis piezoelectric actuated micro motion stage," *IEEE Trans. Ind. Electron.*, vol. 60, no. 11, pp. 5105–5115, Nov. 2013.
- [33] Q. Xu, "Identification and compensation of piezoelectric hysteresis without modeling hysteresis inverse," *IEEE Trans. Ind. Electron.*, vol. 60, no. 9, pp. 3927–3937, Sep. 2013.
- [34] Q. Xu, "Design and development of a compact flexure-based XY precision positioning system with centimeter range," *IEEE Trans. Ind. Electron.*, vol. 61, no. 2, pp. 893–903, Feb. 2014.
- [35] R. Ravaut, G. Lemarquand, V. Lemarquand, and C. Depollier, "Analytical calculation of the magnetic field created by permanent-magnet rings," *IEEE Trans. Magn.*, vol. 44, no. 8, pp. 1982–1989, Aug. 2008.

- [36] R. Ravaut, G. Lemarquand, V. Lemarquand, and C. Depollier, "Permanent magnet couplings: field and torque three-dimensional expressions based on the coulombian model," *IEEE Trans. Magn.*, vol. 45, no. 4, pp. 1950–1958, Apr. 2009.
- [37] S. H. Lee, S. B. Park, S. O. Kwon, J. Y. Lee, J. J. Lee, J. P. Hong, and J. Hur, "Characteristic analysis of the slotless axial-flux type brushless dc motors using image method," *IEEE Trans. Magn.*, vol. 42, no. 4, pp. 1327–1330, Apr. 2006.
- [38] V. H. Nguyen, and W. J. Kim, "Design and control of a compact lightweight planar positioner moving over a concentrated-field magnet matrix," *IEEE/ASME Trans. Mechatronics.*, vol. 18, no. 3, pp. 1090–1099, Jun. 2013.
- [39] V. H. Nguyen, and W. J. Kim, "Novel electromagnetic design for a precision planar positioner moving over a superimposed concentrated-field magnet matrix," *IEEE Trans. Energy Convers.*, vol. 27, no. 1, pp. 52–62, Mar. 2012.



Yinxin Jin was born in Heilongjiang, China. He received the B.E. and M.E. degrees in electrical engineering from the Harbin Institute of Technology (HIT), Harbin, China, in 2010 and 2012, respectively. Since 2012, he has been with the Institute of Electromagnetic and Electronic Technology, HIT, as a doctoral candidate.

His research interests include novel electromagnetic dampers design and optimization research.



He Zhang was born in Heilongjiang, China. He received the B.E. and M.E. degrees in electrical engineering from the Harbin Institute of Technology (HIT), Harbin, China, in 2008 and 2010, respectively. He is currently working toward the Ph.D. degree at the Institute of Electromagnetic and Electronic Technology, HIT.

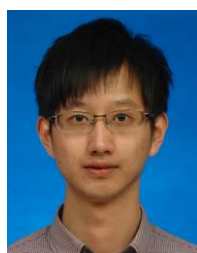
His research interests include magnetic levitation, linear and planar actuators.



Baoquan Kou (M'09) was born in Heilongjiang, China. He received the B.E. and D.E. degrees from the Harbin Institute of Technology (HIT), China, in 1992 and 2004, respectively, and the M.E. degree from Chiba Institute of Technology, Japan, in 1995.

He worked in the mobile station for the post doctors of HIT from 2005 to 2007. Since 2007, he has been a Professor in the School of Electrical Engineering and Automation, HIT. His research interests include electric drive of electric vehicles, linear motors and linear electromagnetic drives,

control of the power quality, and superconducting motors.



Hailin Zhang was born in Chongqing, China. He received the B.E. and M.E. degrees in electrical engineering from the Harbin Institute of Technology (HIT), Harbin, China, in 2010 and 2012, respectively. Since 2012, he has been with the Institute of Electromagnetic and Electronic Technology, HIT, as a doctoral candidate.

His research interests include the high-precision power amplifier and the control of linear motor.